frontiers | Frontiers in Earth Science

TYPE Original Research
PUBLISHED 25 January 2023
DOI 10.3389/feart.2023.1075043

OPEN ACCESS

EDITED BY
Zhong-Hai Li,
University of Chinese Academy of Sciences, China

REVIEWED BY
Yang Chu,
Institute of Geology and Geophysics (CAS), China
Shengsi Sun,
Northwest University, China

*CORRESPONDENCE
Meng-Wan Yeh,
✉ marywyeh@ntnu.edu.tw

SPECIALTY SECTION
This article was submitted to Structural Geology and Tectonics, a section of the journal Frontiers in Earth Science

RECEIVED 20 October 2022
ACCEPTED 03 January 2023
PUBLISHED 25 January 2023

CITATION
Chiu Y-P, Yeh M-W and Lee T-Y (2023), The atypical Gaoligong orocline: Its geodynamic origin and evolution.
Front. Earth Sci. 11:1075043.
doi: 10.3389/feart.2023.1075043

The atypical Gaoligong orocline: Its geodynamic origin and evolution

Yu-Ping Chiu, Meng-Wan Yeh* and Tung-Yi Lee

Department of Earth Sciences, National Taiwan Normal University, Taipei, Taiwan

Various orocline systems around the India–Eurasia collision zone have long been recognized and studied. Different portions of the India–Eurasia boundaries represent various scales and models of orocline-forming processes, such as the Baluchistan orocline formed by multiple deformation events and the Himalayan orocline formed by a mixture of complex structural mechanisms. The curvature from the eastern Himalayan syntaxis through east Burma to west Yunnan showed a unique convex curvature toward the mantle wedge. This is different from the concave Baluchistan orocline and the Himalayan orocline. The unique geometry of the Gaoligong orocline shows an N-S trend for the northern section and a NE-SW trend for the southern section. This curvature also marks the boundary between the Tengchong and Baoshan blocks along the Santaishan suture in western Yunnan, China. Our structural reconstruction identified five deformation events: 1) D_1 is km-scale upright folding, which only affected the Neoproterozoic meta-sedimentary unit, 2) D_2 recumbent folding, which only developed in the southern section of the Gaoligong orocline, 3) D_3 large-scale gently westward-inclined thrust folding, 4) D_4 right-lateral shear belt, and 5) the D_5 normal faults. Since the D_3 structure is the earliest event that shows penetrative foliation development along the orocline, we consider D_1 and D_2 as pre-orocline-forming events. The geometry of the Gaoligong orocline is controlled by the distribution of the Ordovician basement between the Tengchong and Baoshan blocks. Both north and south sections experienced the same structural evolution since D_3 (a fault-propagation fold system occurred between 40 Ma and 28 Ma), D_4 (steep right-lateral shear belt occurred between 28 Ma and 15 Ma), and D_5 (normal faults after 15 Ma). The curvature first developed as a shovel-like top-to-the-NE thrust plane (S_3) that formed under amphibolite-facies conditions between 40 Ma and 28 Ma. The following deformation events (D_4 and D_5) show orocline parallel foliation development under lower metamorphic conditions, indicating that the curvature of the Gaoligong orocline is not generated by additional rotation along multiple deformation events. However, due to the lack of orocline parallel foliation development for S_3, and the lack of a proper position of the indenter, the Gaoligong orocline cannot be classified as a primary orocline nor a rotational orocline. The curved geometry is an interference pattern of topography relief to the shovel-like thrust plane that developed during D_3. Our new reconstructed structural evolution concludes that the Gaoligong orocline is an "atypical" orocline.

KEYWORDS

orocline, shovel-like thrust plane, Gaoligong, Tengchong block, fault-propagation fold

1 Introduction

For centuries, the two geological features people have noticed are tilted rock layers and curved mountain belts. Since deformation was recognized as the result of bending/distortion of once horizontal strata by Sir James Hall during the 19th century, Alpine geologists had long been using structural reconstruction to delineate the four-dimensional geomorphological

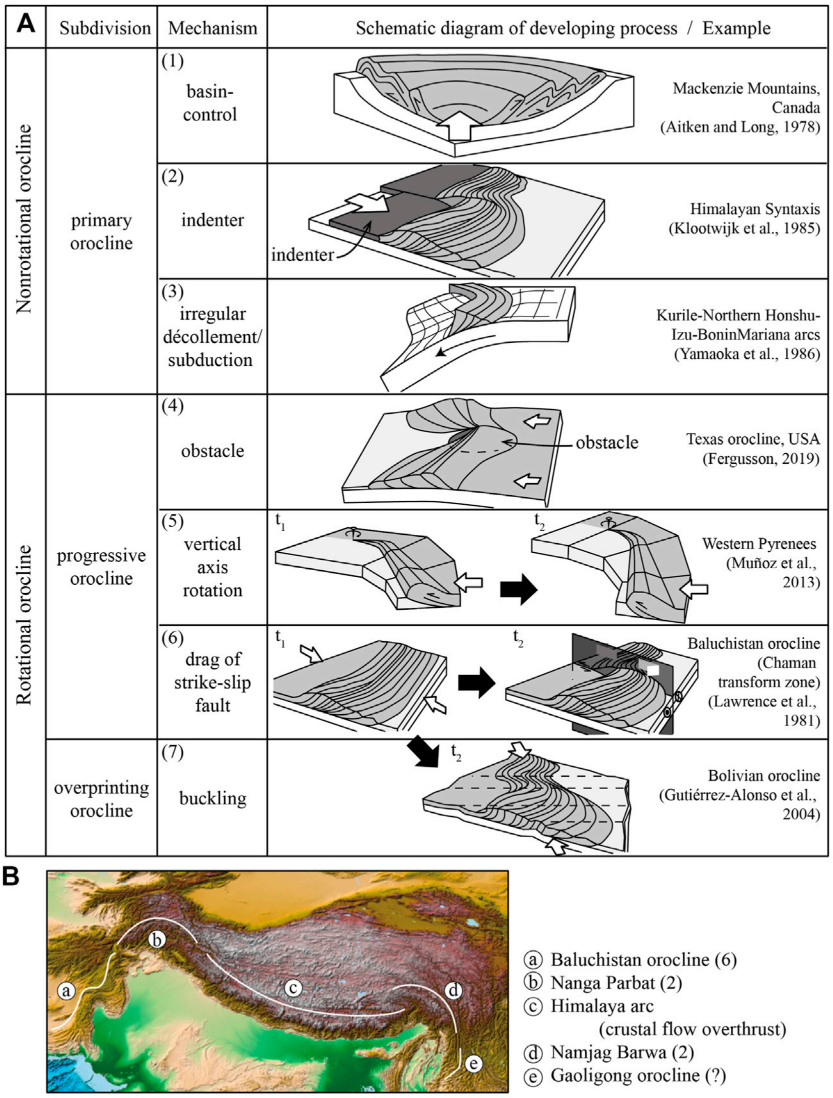

FIGURE 1
(A) Schematic diagrams showing different forming mechanisms and corresponding examples of oroclines. The 3D sketches are modified from Marshak (2005), Hwang et al. (2012), Muñoz et al. (2013),and Bersan et al. (2017). **(B)** ETOPO1 digital relief map around the India–Eurasia collision zone, showing various orocline systems (https://ngdc.noaa.gov/mgg/global/global.html). The numbers mark the type and mechanism that were proposed for its formation by previous studies. No forming mechanism had been proposed for the Gaoligong orocline, from all the orocline systems.

evolution of oroclines through time (Carey, 1955; Sacchi and Cadoppi, 1988; Johnston et al., 2013). They provide windows to understand the complex kinematic interaction system under the evolving stress field of the lithosphere. More research has been conducted over the past decades over numerous oroclines, such as the Alaskan orocline, the Bolivian orocline, the Betic-Rif Belt, the New England orocline, and the Himalayan syntaxes. Recent research interests are more focused on the geodynamic aspects than on the geomorphic/geometric aspects (Bendick and Bilham, 2001; Capitanio et al., 2011; Cawood, 2022).

Several models for primary/non-rotational *versus* progressive/rotational orocline development have been established (Figure 1A; Marshak, 1988; 2005; Weil and Sussman, 2004; Yeh and Bell, 2004; Johnston et al., 2013). The primary/non-rotational orocline reflects the original curvature of the plate boundary without rotation, which is considered to be restricted to thin-skinned thrust belts. The structural characteristic of this subdivision is that only one stage of foliation will develop with different strikes along the orocline. The shape of the primary plate boundary is genetically related to the characteristics of the basin, indenter, or irregularity of basement lithology. The basin-controlled salient (mechanism 1 in Figure 1A) is formed by developing a fold-thrust belt along/within the basin boundary due to uneven sediment thickness (Aitken and Long, 1978; Macedo and Marshak, 1999). For the indentation model (mechanism 2 in Figure 1A), the curvature reflects the geometry of the rigid indenter, such as for the Himalayan syntaxis (Carey, 1955; Klootwijk et al., 1985). The irregularly décollement/subduction model (mechanism 3 in Figure 1A) reflects the heterogeneity in the direction and crustal thickness of décollement/subduction and the variation in the slab thickness (Yamaoka et al., 1986; Macedo and Marshak, 1999; Marshak, 2005; Capitanio et al., 2011).

The progressive/rotational orocline initially forms as a straight mountain belt and is followed by progressive crustal rotation as

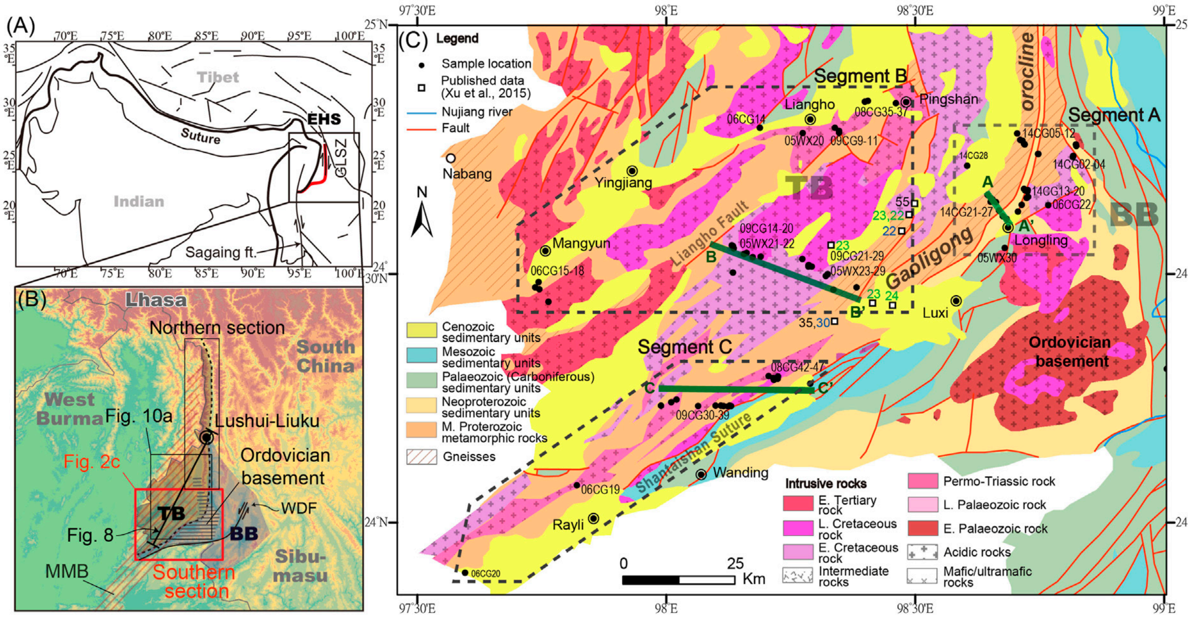

FIGURE 2
Tectonic and geological maps of the study region. **(A)** Sketch diagram showing the general tectonic framework of the oroclines. Most oroclines are convex toward the Indian plate; only the section from EHS to Sagaing fault and the Gaoligong shear zone are convex toward the mantle wedge. The map is modified from Bajolet et al. (2013). **(B)** Topography map with a digital elevation model showing the distribution of the Tengchong block (TB, translucent brown block) and Baoshan block (BB, translucent blue block). The brown hash line marks the Mogok metamorphic block (MMB), and the Ordovician basement is marked by the gray horizontal line (Ye et al., 2020). WDF—Wanding fault. **(C)** Geological map of the Gaoligong orocline showing lithology units, fault distributions, cross-sections, and sample location. The published ages are quoted from Xu et al. (2015). The black number marks the age of zircon U-Pb dating, the blue marks the age of hornblende Ar–Ar dating, and the green marks the age of biotite Ar–Ar dating. The map is modified from BGMRYP (1983), Ma et al. (2014), and Xu et al. (2012).

plate–scale interactions among the crust and lithospheric mantle occur (Johnston et al., 2013). Therefore, the formation of an orocline would accompany multiple deformation events with multiple cross-cutting foliation developments. Three crust rotation styles are further classified as obstacle (mechanism 4 in Figure 1A), vertical axis rotation (mechanism 5 in Figure 1A), and drag of strike-slip fault (mechanism 6 in Figure 1A). The obstacle-produced model (mechanism 4) considers the curvature of a fold-thrust belt and is enhanced as it bends around a strong impeded obstacle such as a seamount (Marshak, 1988; Macedo and Marshak, 1999; Marshak, 2005). The Texas orocline is an example as it is formed by the subduction of a seamount chain (Fergusson, 2019). Both the vertical axis-rotated model and the drag of the strike-slip shearing model (mechanisms 5 and 6) are related to horizontal non-coaxial deformation but under different faulting mechanisms. The vertical axis-rotated model (mechanism 5) was developed based on the detachment/décollement propagating during the vertical axis rotation of the Iberian Peninsula about a pivot in the Western Pyrenees (Carey, 1955). The drag of the strike-slip shearing model (mechanism 6; Marshak, 1988; Macedo and Marshak, 1999) describes the formation of an orocline as a once straight fold-thrust belt that is later sheared into multiple curved fold-thrust belts, such as the Variscan orocline in the Western Alps (Martínez Catalán, 2011) and Chaman transform zone for the Baluchistan orocline in Pakistan (Lawrence et al., 1981).

The overprinting orocline (mechanism 7 in Figure 1A) is formed by alternating the stress direction. As the stress direction of later deformation becomes parallel to the trend of the pre-existing fold-thrust belt, the pre-existing fold-thrust belt is then bent or buckled (Macedo and Marshak, 1999; Marshak, 2005). In the cases of the Bolivian orocline of the Andes (Gutiérrez-Alonso et al., 2004) and the Cantabrian orocline of the Pyrenees (Weil et al., 2001; Gutiérrez-Alonso et al., 2012), the buckling process thickened the curst by adding a strip of oceanic crust into a continental matrix, causing delamination of the lithospheric root under the inner arc region (Gutiérrez-Alonso et al., 2004). A few oroclines were likely affected by multiple mechanisms. The Serra Central Salient of eastern Brazil was formed by a hybrid of non-rotational orocline, followed by vertical axis rotation (Bersan et al., 2017). Another case is the Central Iberian arc that was controlled by progressive and overprinting models (shearing and buckling; Martínez Catalán, 2012).

The Gaoligong orocline is the southeastern stretch of the large-scale curvature of the Himalayan orocline, which marks the general boundary between Eurasia and India plates (Figure 1B). The orocline's shape is generally concave to the subducting plates. As Bajolet et al. (2013) have pointed out, the Himalayan orocline curvature and syntaxes are a unique and present oddity as the curvature is convex toward the subducting plate (India). The Himalayan section shows a concave curvature to the subducting plates and extends from both the western and eastern syntaxes that include the Zagros thrust belt and the Gaoligong orocline. The existence of the Gaoligong orocline has long been recognized, and its structural evolution has been debated for an equally long period (Y.G. Wang et al., 2006a; Song et al., 2010; Eroglu et al., 2013; Xu et al., 2015; Zhang et al., 2017; Chiu et al., 2018). Previous studies mostly focus on reconstructing the detailed evolution of either the northern or the southern section of the Gaoligong orogen, but not the Gaoligong orocline. Furthermore, the structural evolution for the northern and southern sections has not

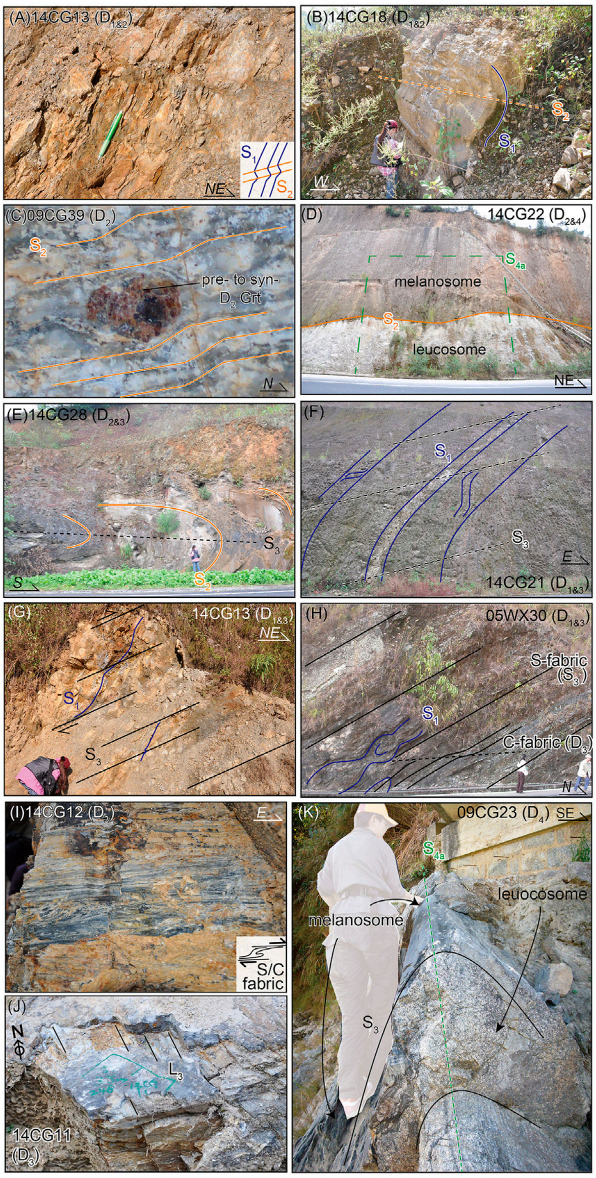

FIGURE 3
Outcrop photos and sketches showing the structural style and fold interference patterns for different deformation events. Photos **(A–D)** are D_2-related structures from low to high strain. Photos **(E–H)** show D_3-related structures with shallow to steep dips and increasing metamorphic grades. **(A)** D_2 N-S-striking sub-horizontal shear plane with the S_1 kink bend. **(B)** Recumbent folds (S_1) with a sub-horizontal fold axial plane (S_2). **(C)** Garnet-bearing mylonitic gneiss showing an N-S-striking sub-horizontal foliation (S_2) under the upper amphibolite to granulite facies. **(D)** Contact between melanosome and leucosome is parallel to the N-S-striking sub-horizontal foliation (S_2), suggesting the migmatization is syn-D_2 under granulite facies. **(E)** D_3 thrust ramp folds forming a NW-SE-striking sub-horizontal fold axial plane (S_3). **(F)** Recumbent folds of slate outcrop with a weakly developed fold axial plane (S_3). **(G)** S_3 fabric showing a thrust sense of shear. **(H)** Outcrop preserving isoclinal D_1 fold with a fold axial plane parallel to the dominant NW-SE-striking SW-dipping matrix foliation (S_3), a penetrative sub-horizontal shear plane **(C)** can be noted to develop at the bottom of the outcrop. **(I)** Mylonite preserves the sense of thrust for the D_3 shear zone. **(J)** N-S-trending L_3 shows on the shear plane of D_3 around the Ordovician basement. **(K)** Outcrop preserving D_3 shear plane folded into the isoclinal D_{4a} fold with NE-SW-striking, NW-dipping fold axial plane (S_{4a}).

been correlated or compared. This is crucial in order to delineate the orocline formation mechanism. For this study, we compare and contrast the structural evolution history of the northern and southern sections to determine the timing and mechanism of the Gaoligong orocline formation.

2 Geological setting

The 20-km wide, 400-km long Gaoligong orocline marks the boundary between the Tengchong and Baoshan blocks (Figures 2A, B). The teleseismic waveform data from temporary broadband seismometers show a difference between the crustal thicknesses of the two blocks. The crust of the Baoshan block (35 km–30 km) is slightly thinner than that of the Tengchong block (35 km–40 km; Zhang and Gao, 2019). The basement of the Tengchong block can further extend southward to the basement of the Mogok metamorphic belt (MMB; Figure 2B; Shi et al., 2011). Both Tengchong and Baoshan blocks are composed of Paleoproterozoic metamorphic and Neoproterozoic sedimentary units (Shi et al., 2011). These blocks are situated at the active volcanic rift setting of the Australian margin of Gondwana before the middle Early Permian (Metcalfe, 1996; Wopfner, 1996; Sone and Metcalfe, 2008; Liu et al., 2009; Liu et al., 2021). At ~500 Ma, the southward-subducted Proto-Tethys slab started to roll back, which induced a back-arc basin formation. The breakoff of the slab around 490 Ma–467 Ma led to basin closure, accompanied by multiple magmatic events (Wang et al., 2013; Zhao et al., 2014; Li et al., 2016; Zhao et al., 2017; Dan et al., 2022). These sedimentary units and the magmatic batholiths composed the Ordovician basement between the Tengchong and Baoshan blocks (Figure 2B; Wang et al., 2013; Zhao et al., 2014; Li et al., 2016; Zhao et al., 2017).

Both Tengchong and Baoshan blocks were individually separated from Gondwana during the Early Permian (Wopfner, 1996; Metcalfe, 2013). They were later sutured together before the Early Cretaceous (Qi et al., 2019). Starting from the Late Cretaceous until the Paleocene, the S-type granites showed a gradual westward younging trend toward the boundary of the Tengchong block (Zhang et al., 2017; Sun et al., 2020). The I-type granitoids intruded along the western margin of the Tengchong block until ~50 Ma, which can be correlated to the Gangdese arc belt as the Neo-Tethys slab subducted beneath Eurasia (Figure 2C; Xu et al., 2012; Ma et al., 2014). The stress regime switched from compression to extension between 53 and 40 Ma. A 53-Ma A_2-type granite extends from the central to western Tengchong block, formed under a back-arc extensional setting (Chen et al., 2015). The magmatic flare-up was likely due to the breakoff of the Neo-Tethys slab and increased the contribution of mantle-derived melts until the emplacement of intraplate-type basaltic dykes at ~40 Ma in the central region of the Tengchong block (Xu et al., 2008; Xie et al., 2016).

The Gaoligong shear zone (GLSZ) and Santaishan suture mark the boundaries between Tengchong and Baoshan blocks. In this study, we defined the N-S trending Gaoligong orogen along the GLSZ as the northern section of the Gaoligong orocline and NE-SW trending region as the southern section (Figure 2B). Chiu et al. (2018) revealed four ductile deformation events for the northern section.

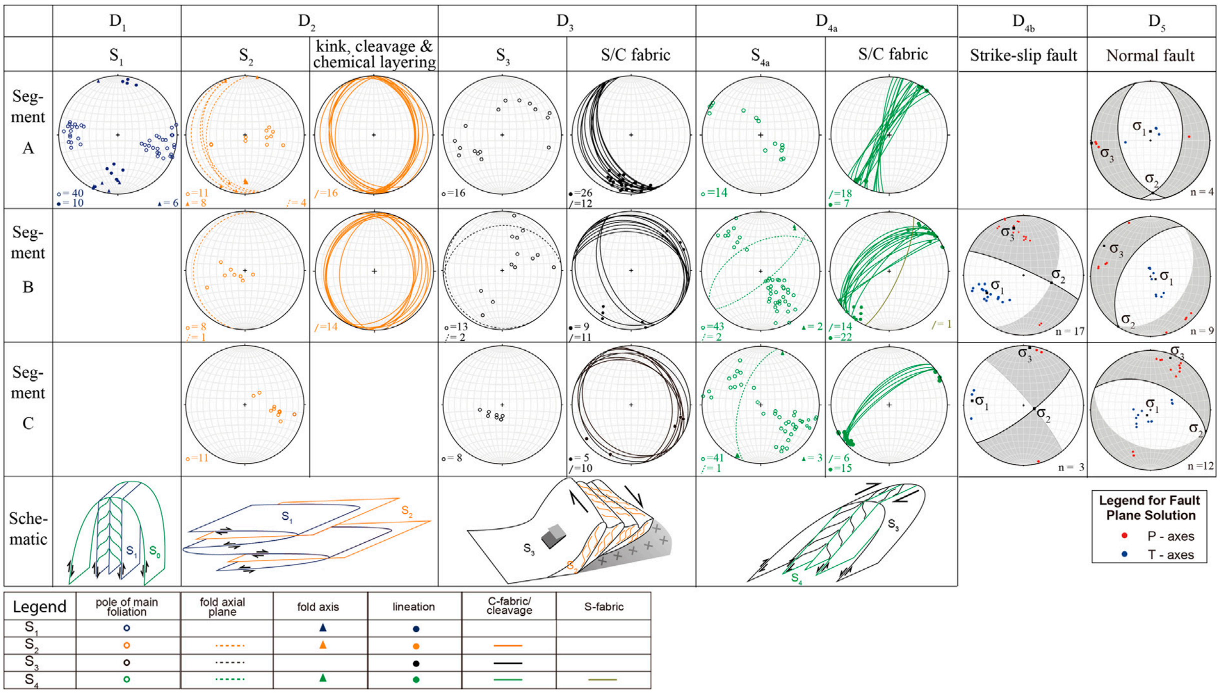

FIGURE 4
Southern hemisphere equal-area projection of field measurements separated according to ductile deformation events from D_1, D_2, D_3, and D_{4a} of three sections A, B, and C. Simplified structural pattern sketches of D_1 to D_4 are provided at the bottom. Various colors mark different foliations. Mylonitic S/C and S/C_1 fabrics are separated from matrix foliation for D_3 and D_{4a}, respectively. Open circles mark the poles of all foliations, solid triangles mark the fold axis, and solid circles mark the mineral stretching lineation. Dash lines mark the fold axial plane, and solid lines mark the cleavages. (B) Fault kinematic solutions of brittle events (D_{4b} and D_5) plotted with equal-area southern hemisphere stereographic projection. The list of field measurement data is provided in Supplementary Table S1.

D_1 formed the WNW-ESE-striking upright folds that are interpreted as resulting from the closure of the Neo-Tethyan ocean during the Early Cretaceous (118 Ma–78 Ma). D_2 caused large-scale eastward thrusting and folding with a top-to-the-N/NE sense of shearing under upper-amphibolite-facies conditions between 50 Ma and 35 Ma. D_3 formed a moderate NE-dipping, NW-SE-striking, and left-lateral shear zone under middle-to-lower-amphibolite-facies metamorphic conditions that accommodated the southeastward extrusion of Indochina around 35 Ma–28 Ma. D_4 caused sub-vertical right-lateral shearing of the GLSZ in the evident N-S trend and retrograded from amphibolite facies into greenschist facies during 28 Ma–15 Ma.

The Gaoligong orocline bends to the NE-SW along the Santaishan suture (Figures 2B, C; Qi et al., 2019). Mitchell et al. (2008) refer to it as the Luxi–Namkham suture and further connects it to the suture of the Paung Laung–Mawchi zone along the Shan boundary. Zhang et al. (2017) reported four ductile deformation events: D_1 is the large-scale top-to-the-east sub-horizontal thrust during 114 Ma–104 Ma. D_2 is an intrusion doming event during 67 Ma–30 Ma. The magmatism caused the migmatization of the host rock and triggered a thrust-fault belt on the top of the dome structure. The contacts between granite, granitic mylonite, mylonite, phyllite, and sedimentary rocks are mostly sub-horizontal, parallel to the flat-laying thrusting detachment (Xu et al., 2015), indicating that major metamorphic layering and differentiation occurred during this event. Minor strike-slip shear belts are developed along both limbs of the dome structure. These strike-slip shear belts are further developed by the following deformation event (D_3) under the right-lateral shear condition that can correspond to the N-S-trending right-lateral shear event (D_4) of the north section (which is D_3 for Zhang et al., 2017; Chiu et al., 2018). By correlating each deformation event to our new data for the southern section and comparing that to the previously studied northern section, we can re-establish a new structural evolution of the southern section of the Gaoligong orocline and delineate which deformation event had caused the formation of the Gaoligong orocline.

3 Results and interpretations

3.1 Reconstructed structural evolution of the southern section of the Gaoligong orocline

Based on cross-cutting relationships observed in the field and oriented thin sections, the succession of four ductile deformation events (D_1, D_2, D_3, and D_{4a}), with D_{4b} marking the ductile-brittle transition event, followed by a brittle deformation (D_5) event, were recognized along the three segments (Figures 3–6). D_1 and D_2 are folding events, while both D_3 and D_{4a} are shearing events with folds of different oriented shear (S/C) fabrics.

3.1.1 D_1

The oldest event, D_1, formed km-scale upright open folds with N-S-striking and sub-vertical axial plane S_1 (between 345°–028°, an

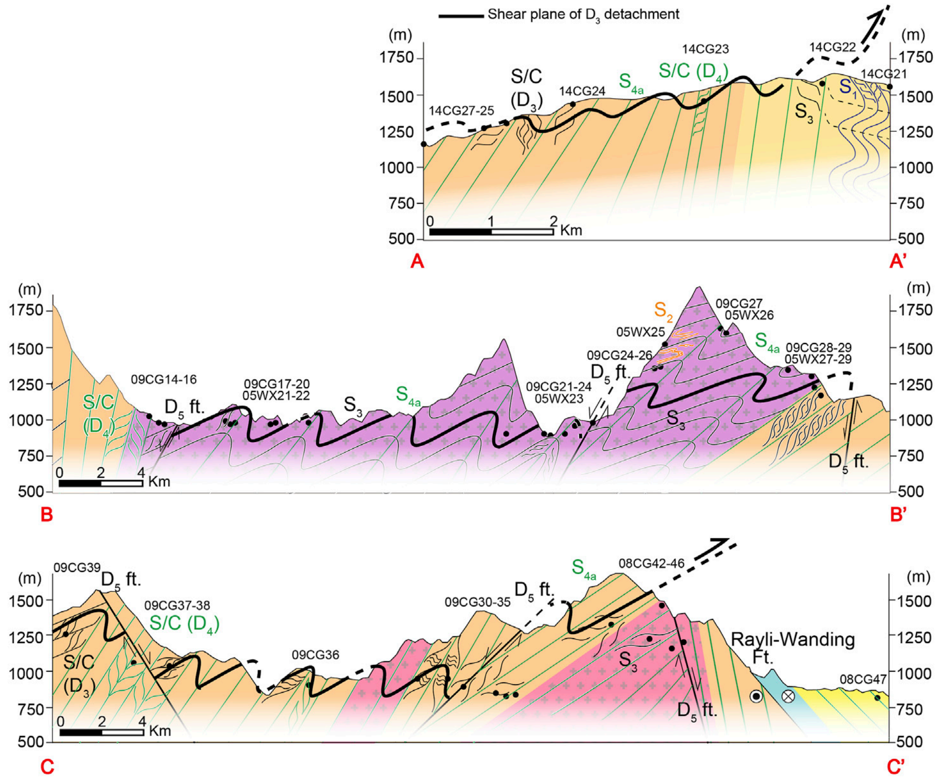

FIGURE 5
Reconstructed cross-sections of **(A,A′)**, **(B,B′)**, and **(C,C′)** segments. The oldest D_1 fold formed the S_1 axial plane (blue lines). D_2 formed the sub-horizontal S_2 foliation and chemical layering (orange lines). D_3 thrust shear folding formed the S_3 fold axial plane (black). The thick black line marks the shear plane of the D_3 fold-thrust belt. The D_4 shear fabrics (green) deformed multiple rock units, and the early stage of D_4 (D_{4a}) folded D_3 thrust shear belts, forming the S_{4a} axial plane (green) and then transformed into brittle deformation (D_{4b}). The latest normal fault (thick gray line), D_5, truncated all ductile fabrics.

average value of 010°; Figures 3A, B; Figure 4; Figure 5). All D_1 structures are observed within the Neoproterozoic meta-sedimentary unit (Figure 5). The S_1 within the meta-sedimentary unit was later deformed by D_2 and D_3 fold axial planes, away from the highly deformed region of the D_3 thrust plane (Figures 3A, B, F). Petrographic analysis shows that the S_1 is defined by mica folia and quartz ribbons with a right-lateral sense of shear (Figure 6A). The grain boundary migration of the quartz ribbon indicates a temperature range >500°C (Figure 6A), and the bulging of feldspar (Figure 6B) further constrains the metamorphic conditions from middle-to-lower amphibolite facies (>600°C; Passchier and Trouw, 1996; Owona et al., 2013).

3.1.2 D_2

D_2 forms meter-scale recumbent folds with the N-S-trending sub-horizontal fold axial plane cleavages (S_2, Figures 3B, 4). Clear metamorphic layering showing a wide range of metamorphic conditions can be observed along different altitude outcrops. Lower-grade metamorphic conditions of brittly kinked mica-bearing D_1-related phyllonite within the meta-sedimentary unit are observed at a higher altitude (~2,000 m; Figure 3A), whereas medium-to-high-grade metamorphism indicated by sillimanite–garnet-bearing mylonitic gneiss is observed for outcrops at lower altitudes (~1,200 m; Figure 3C). Strong metamorphic layering with a segregated quartzo–feldspathic-rich layer and a mica–sillimanite-rich layer can be observed for lower-altitude regions. Furthermore, sub-horizontal N-S-trending leucosome sheets can also be observed at lower-altitude outcrops (Figure 3D), indicating that the metamorphic condition of D_2 could be as high as granulite facies. Even though the melanosome and leucosome have developed S_3 during the later thrusting event, the contact still maintains the characteristics of D_2, which is N-S trending. The vertical variation of metamorphic conditions from high-grade metamorphism at outcrops from 1,000-meter elevation to low-grade metamorphism at outcrops from 2,000-meter elevation showed that a much higher geothermal gradient is required if no structural deformation had occurred to displace rocks. Thrust faults tend to bring deeper rocks up for the hanging wall, whereas normal faults tend to push upper rocks down for the hanging wall. Since most of the outcrops we observed belong to the hanging wall and low-grade metamorphic rocks are observed for higher altitudes, we determined that these recumbent folds should accompany an extensional setting such as normal listric faulting conditions for D_2.

3.1.3 D_3

D_3 is a thrust folding event that reactivated recumbent D_2 folds to form large-scale sub-horizontal to gently westward-inclined folds (Figure 3; Figure 4) along a "listric type" thrust ramp. A dominant top-to-the-NE sense of shear NW-SE-striking, shallow SE dipping S_3 fold axial planes can be noted (Figure 4). The dip (5°–55°) of S_3 foliation showed systematic variation at different altitudes; the higher the elevation, the steeper the dip for S_3 (Figure 5). Concentrated well-developed S-C fabrics are noted for narrow mylonitic belts at lower-altitude outcrops under high-grade metamorphic conditions

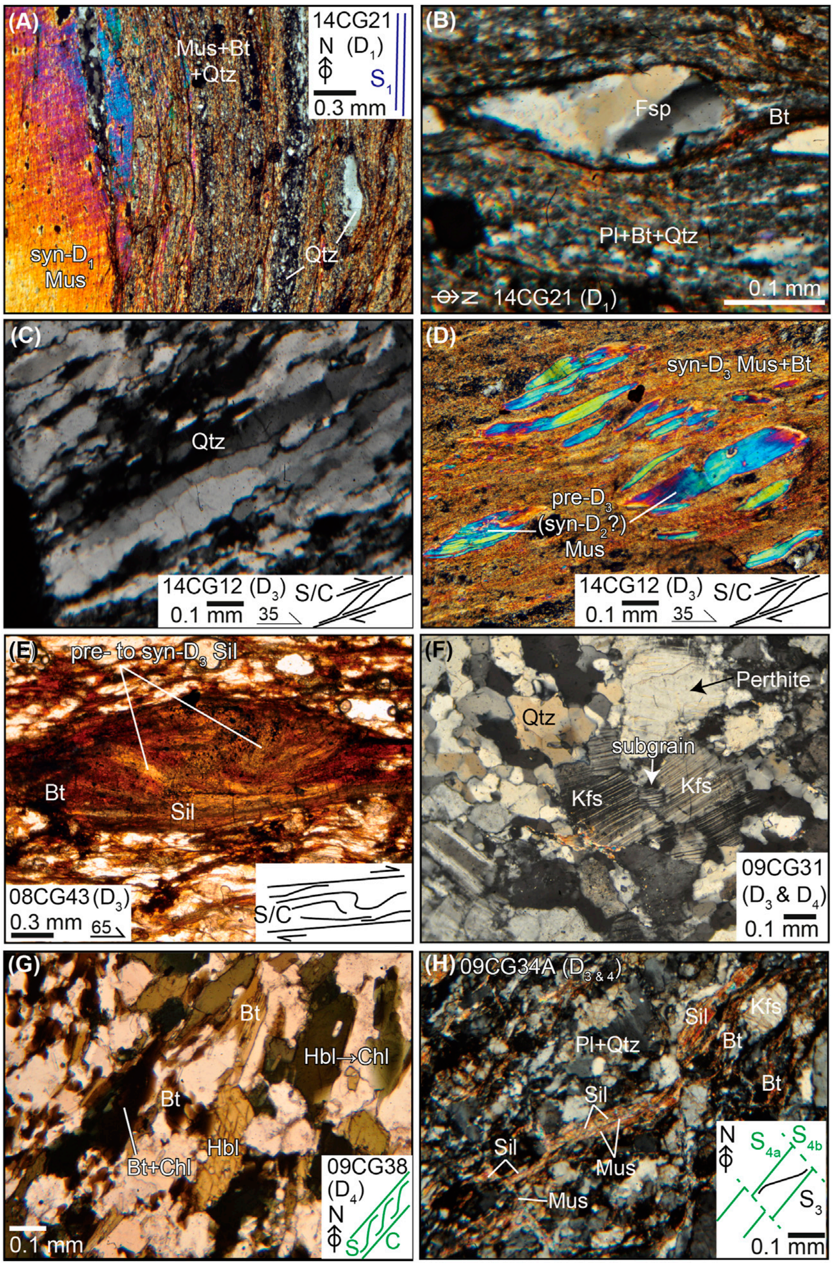

FIGURE 6
Microphotographs illustrating the microstructural and petrological relationship of D_1 to D_4. **(A)** Mylonitic S_1 fabric with a right-lateral sense of shear defined by mica folia and very fine-grained quartz + feldspar aggregates in the ribbon. The deformation mechanism of the relic of quartz ribbon (the left side) is the grain boundary migration. **(B)** Right-lateral sense of shear of D_1 can be indicated by the biotite, which wrapped the pressure shadow of the bulged K-feldspar with undulose extinction. **(C)** Grain boundary migration of quartz was observed from the C-fabric-parallel ribbon with undulose extinction. **(D)** Mylonitic S/C fabric is defined by muscovite + biotite folia and mica fish with a sub-horizontal thrust component. **(E)** Mylonitic S/C fabric is defined by biotite folia. The biotite fish contain folded sillimanite inclusions. **(F)** Microphotograph showing pre- to syn-D_3 subgrain-rotated K-feldspar. **(G)** Mylonitic S/C_1 fabric is defined by chlorite + biotite ± chloritized hornblende with a dextral sense of shear. **(H)** S_3 is defined by sillimanite folia, which are bound by NE-SW-striking S_{4a} foliation defined by fine-grained muscovite and plagioclase and quartz aggregates. Truncation and offsets of both S_3 and S_{4a} by S_{4b} fractures can be noted. Bt, biotite; Chl, chlorite; Fap, feldspar; Hbl, hornblende; Kfs, K-feldspar; Mus, muscovite; Pl, plagioclase; Qtz, quartz; and Sil, sillimanite.

(Figure 3I) along the thrust ramp. The mineral assemblage of muscovite + biotite + sillimanite and quartz ribbons (Figures 6C–E) is observed for the S-C fabric, which is indicative of amphibolite-facies metamorphism (Barrow, 1893). Sub-grain-rotation of feldspar (Figure 6F) indicates a temperature of up to 700°C (Passchier and Trouw, 1996; Owona et al., 2013). This medium-to-high-temperature metamorphism is accompanied by hydrous minerals, such as muscovite, biotite (Figures 6D, E), and hornblende (Figure 6G), which could result in syn-kinematic melting of anatexis (Patino Douce et al., 1990), thus responsible for the thick leucosome of migmatite that appears along the thrust ramp.

Strong strain-partitioning patterns are observed throughout the study region. Older fabrics are better preserved for the less-strained regions as the D_3 C-fabrics are poorly developed, whereas

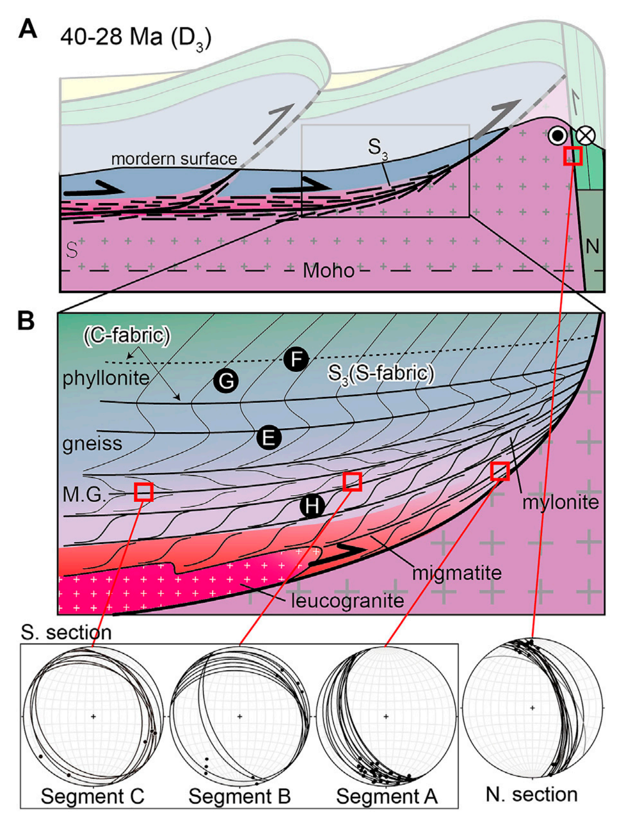

FIGURE 7
Schematic diagram with southern hemisphere equal-area projection stereonet diagram showing geographical distribution of reconstructed S_3 foliation with various dip and metamorphic conditions of the D_3 fold and thrust complex. **(A)** Sub-horizontal to gentle back-limb produces a significant horizontal shearing and folding at higher metamorphic conditions. The steep fore-limb developed the sub-vertical strike-slip fault against the boundary of the Baoshan block as the Ordovician basement prevented stress penetration. **(B)** Schematic diagram showing the structural pattern and relative outcrop altitude labeled as a black circle with text, which correspond to the outcrop photos in Figure 3. The distribution of rock types changed from leucogranite, migmatite, migmatitic gneiss [M. G.], gneiss, and phyllonite toward the top. A higher strain is observed for the lower portion under higher metamorphic conditions. The red square marks the relative position of S_3 foliation measurements, showing sub-horizontal to steep NE-dipping trend.

the S-fabrics are more dominantly observed from the outcrop (Figures 3F–H). Similar to the S_3 fabrics, the upper portion of the fold-thrust belt shows a steeper dip of C-fabrics (40°) than that for the lower portion with a shallower dip of C-fabrics (11°). The curved shear plane cropped out at different elevations from the west at around 800 m–1,000 m of altitude to the east that climbed from ~1,200 m to ~2,000 m (2,075 m is the location of sample 14CG12; the thick black line in Figure 5). A clear spatial pattern of strain condition, structural style, and metamorphic condition can be drawn for the D_3 event. With higher altitude outcrop, less strained low metamorphic grade meta-sedimentary rocks are observed which preserved the older S_1 and S_2 fabrics (Figures 3E–G). In contrast, With lower altitude outcrop, hornblende, gneiss, and mylonitic gneiss rocks are highly strained under medium-to-high-grade metamorphism accompanied by the symmetric sub-horizontal stretching lineation (Figure 7).

3.1.4 D_4

D_4 is a NE-SW-striking steep NW-dipping right-lateral shearing event that can be further divided into two stages: the ductile D_{4a} (Figure 4; Figure 6H) and the brittle D_{4b} (Figure 4). The dip of the shear plane becomes steeper from 45° to 90° from the southwest region toward the northeast region. The D_{4a} right-lateral shearing event accompanied inclined shear folding with NE-SW-striking (22°–55°, the average value is 41.9°; Figure 4), steeply NW-dipping fold axial plane (S_4) under a more ductile regime. This event strongly deformed the earlier fabrics (Figure 3K), including folding the D_3 detachment (the black thick line in Figure 5). Figure 3K shows that the mylonitic melanosome with the D_3 shear sense is folded by the D_4-inclined fold. The S-C_1 shear fabrics are dominated by quartz + biotite + chlorite + tourmaline ± muscovite ± sphene (Figure 6G; Supplementary Table S2) with NE-trending sub-horizontal mineral-stretching lineation L_{4a}. The boudinaged syn-D_2 sillimanite is included in S_4 muscovite (Figure 6H), indicating that a retrograde metamorphism had occurred from D_2 to D_4. This retrograde condition continued to lower greenschist facies according to the chloritization of S_{4a}-parallel biotite and sub-hedral hornblende fragments (Figure 6G). Recrystallized chlorite folia indicate that the D_{4a} shearing event occurred under lower greenschist facies conditions (250°C–400°C).

The lowest temperature of D_4 deformation can be constrained by the development of brittle deformation of D_{4b} (Figure 4). A conjugate fault system of the NE-SW right-lateral and NW-SE left-lateral system was observed and measured (Figure 4; Figure 5; Figure 6H). On the outcrop, the NE-SW right-lateral faults are the dominant fault observed, which is also parallel to the shear plane (C_1) of D_{4a} (Figures 4, 5). The conjugate NW-SE-striking left-lateral fault can also be observed under thin sections as muscovite grains (S_{4b}) truncate the S_{4a} fabric (Figure 6H). The fault kinematic solution results show that the D_{4b} brittle faults formed under a SW-dipping σ_1, E-dipping σ_2, and subhorizontal N- (or S-) trending σ_3 stress regime (Figure 4). Consequently, the NE-SW-striking dextral shearing of the D_4 initially occurred under mid-crustal-level conditions and progressively propagated toward the surface.

3.1.5 D_5

The latest structural features observed are a series of Gaoligong orocline–parallel normal faults (Figure 4) that truncated all ductile fabrics and further rugged the topography (Figure 5). The fault kinematic solution results show sub-vertical σ_1, sub-horizontal N-S trending σ_2, and sub-horizontal E-W trending σ_3 for the formation of these normal faults, and σ_1 and σ_3 exchanged their orientation in the southwest margin of the Tengchong block (Figure 4).

3.2 The correlation of structural evolution among the northern and southern sections

Based on our structural reconstruction, the D_5 normal faults are observed from the northern (Chiu et al., 2018) and southern sections. Although the fault strikes differently among the two sections, the reconstructed fault kinematic analysis and the thermal history are the same for both sections. Xu et al. (2015) obtained the Ar–Ar age plateau of biotite at ca. 23 Ma in the southern section of the Gaoligong orocline (Figure 2C), which is similar to the age in the northern section (Chiu et al., 2018). This indicates that the southern and northern segments have the same thermal history. It should be logical to correlate the

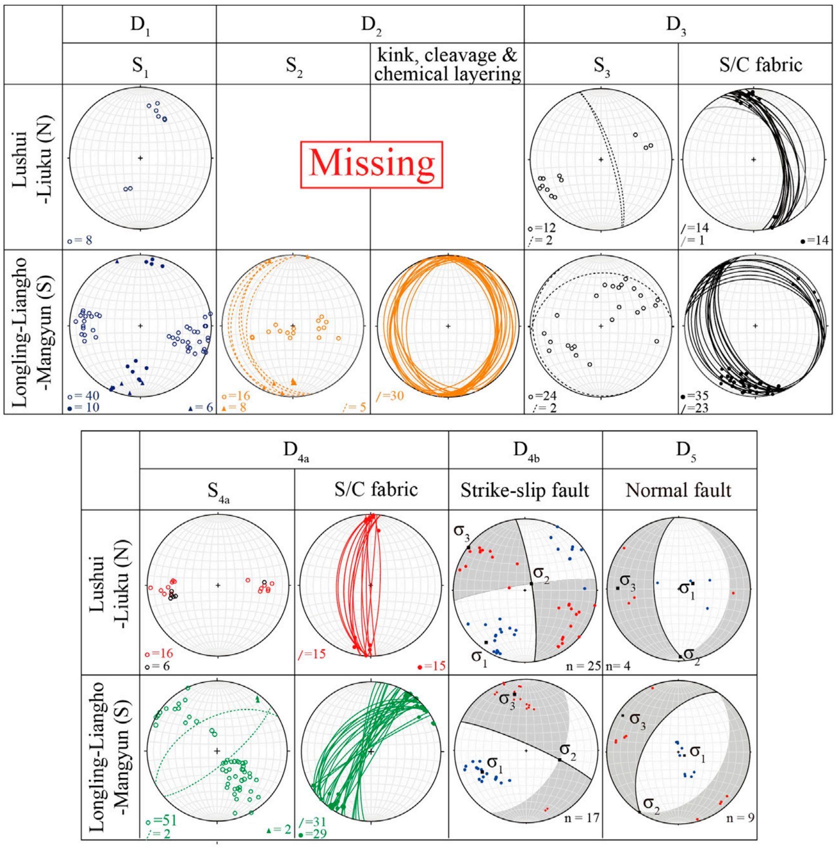

FIGURE 8
Diagram showing southern hemisphere equal-area projection stereonet diagrams of each reconstructed deformation event from both northern (Lushui–Liuku; Chiu et al., 2018) and southern (Longling–Liangho–Mangyun; this study) segments of the Gaoligong orocline. D_3, D_4, and D_5 can be correlated as the same events for both northern and southern sections according to the same structural style and stress pattern. D_2 from the southern section, however, cannot be correlated to any deformation events in the northern section. Therefore, we assume that D_2 only affected the southern section. Although D_1 from both sections shows some similarity in the foliation style, we do not consider the correlation to be formed due to too few data.

same age ranges for D_4 and D_5 as Chiu et al. (2018) suggested. On the premise that the D_4 deformation temperature is close to the closure temperature of the feldspar, Chiu et al. (2018) adopted the younger age of the microcline feldspar as the lower limit of D_4 (15 Ma). The younger age is similar to the start of normal faulting within the Tengchong block (G. Wang et al., 2006). As the fault strikes followed the orocline, the orocline had already formed prior to D_5 (Figure 8). Similar reasoning can be applied to D_4. As D_4 defines the sub-vertical right-lateral strike-slip shear zone developed along the curvature of the Gaoligong orocline, we correlated D_4 from both sections as the same event. This makes D_4 the most dominant right-lateral shearing of the Gaoligong shear belt at this time (28 Ma–15 Ma) and indicates that it was formulated after the formation of the Gaoligong orocline (Figure 8; Chiu et al., 2018).

Unlike D_4 and D_5, D_3 is the first event that did not show structure orientation that follows the trend of the orocline. D_3 in the northern section forms a NW-SE-striking steeply NE dipping thrust belt with a sinistral sense of shear during 35 Ma–28 Ma (Chiu et al., 2018). Although D_3 in the southern section is also a thrusting event, the thrust boundary shows a general NW-SE strike but shallow NE-SW dip direction (Figure 8). A spatial pattern of the steeper dip of the shear plane (C_1) corresponds to the lower metamorphic grade and higher altitude toward the eastern boundary of the Tengchong block as is noted for D_3 (Figure 7B). If we consider the D_3 from the northern and southern sections as the same thrusting event, a shovel-like thrusting plane and curved fold-thrust belt can be recognized that is similar to a fault-propagation fold system (Figure 7A). The various dip directions of the C_1-fabrics can be explained geographically as the northern section marks the footwall of the thrust system. Hence, the NE-dipping steep C_1 foliation observed from the northern section defines the forelimb of the fault propagation fold system (Figure 7A). The shallow-to-moderate dipping C_1 foliations observed from the southern section is equivalent to the flat shear plan to the ramp of this thrust system (Figure 7B).

Other than a spatial pattern between S_3 and C_1 foliations, a spatial pattern can also be observed for the mineral stretching lineation of the mylonites (L_3). Based on Figure 7B, the mineral stretching lineation changed from broad NE-SW plunging to S-plunging and then to N-plunging in mylonitic layers (Figure 3J; Figure 4). This spatial variation in lineation shows the presence of a regional structure along the boundary east of the thrust front which blocked the propagation of strain. Since the D_3 event shows strong spatial variation of foliation, mineral stretching lineation, and metamorphic conditions, we suggest this should be the event that produced the Gaoligong orocline. Recumbent folding under the extensional regime (D_2) is not noted for the northern

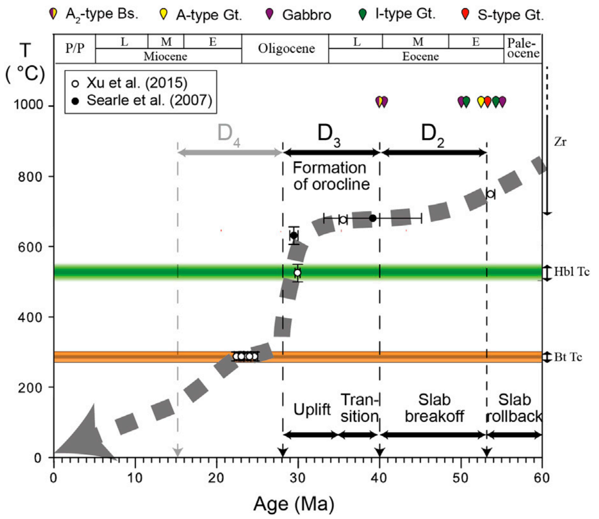

FIGURE 9
Reconstructed cooling path according to published ages and their closure temperature/thermal conditions. The ages are zircon U-Pb dating ages with Ti-in-zircon thermometry, the Ar–Ar ages of hornblende and biotite (Xu et al., 2015), and monazite U-Pb ages with the garnet–biotite geothermometer from the Mogok metamorphic belt (Searle et al., 2007). The different color symbols at 1,000°C mark different magmatic periods of I-type, S-type, A-type, and gabbro in the Tengchong block. Combining the cooling path, the tectonic evolution, and medium-to-high-grade metamorphism conditions for D_2 and D_3, we considered that D_2 occurred during 53–40 Ma when the extensional setting caused the slow cooling of the rock as leucogranite formed. D_3 occurred during 40–28 Ma when the compressional setting produced a thrust fold belt followed by rapid cooling with the uplift, which is D_4. The closure temperatures (T_C) of different minerals used are as follows: T_{CHbl} for hornblende (500°C–550°C; Harrison and McDougall, 1982), T_{CBt} for biotite (275°C–300°C; Harrison et al., 1985); Gt, granite; Bs, basalt; L, late; M, middle; E, early; Paleo, Paleocene; P/P, Pliocene to present.

section. Therefore, we considered the D_2 event as a local event that only occurred in the southern section (Figure 8). Although earlier D_1 events are noted for both sections, insufficient information on neither the structural style nor stress pattern can be used for correlation. Therefore, we only correlate the structural evolution of the whole Gaoligong orocline from D_3 to D_5.

4 Discussion

4.1 The timing of Gaoligong orocline formation

With careful examination of the structural evolution of the Gaoligong orocline, we have revealed that the northern section (Chiu et al., 2018) and the southern section (this study) of the Tengchong block underwent the same structural evolution from D_3 to D_5. With D_4 and D_5 having the same structural trends of the orocline but not D_3, we assigned D_3 to the formulation of the Gaoligong orocline around 40–28 Ma. If we examine the tectonic kinematic setting of the Tengchong block during this time, we can see that the tectonic stress condition changed from extension to compression as the hard collision between India and Eurasia occurred around 40 Ma (Figure 9; Chung et al., 2005; Xu et al., 2008). Before 40 Ma, the Tengchong block was a back-arc setting since 65 Ma due to the rollback of the Neo-Tethys slab (He et al., 2021). This extensional condition continued until slab breakoff occurred around 40 Ma (Xu et al., 2008), making it less likely to form a compressional orocline. The continued northward propagation of the West Burma terrane after 28 Ma (Mitchell, 1993; Gardiner et al., 2018; Morley and Arboit, 2019) is complementary to the further delamination and uplifting of the Tibetan Plateau (Chung et al., 2005). The tectonic strain condition changed to block rotation along the Eastern Himalayan syntaxis and development of N-S-trending dextral shear zones (Chiu et al., 2018). The middle-to-lower-crustal level flow around the Eastern Himalayan syntaxis (Royden et al., 1997; Clark and Royden, 2000; Burchfiel, 2004) is considered as the dominant mechanism for the development of these strike-slip shear zones (D_4). Such a stress condition can reactivate the already deformed thrust plane (S_3) into penetrative shear belts with curvature but not forming a curved shear belt. By comparing the reconstructed structural evolution among the northern and southern sections of

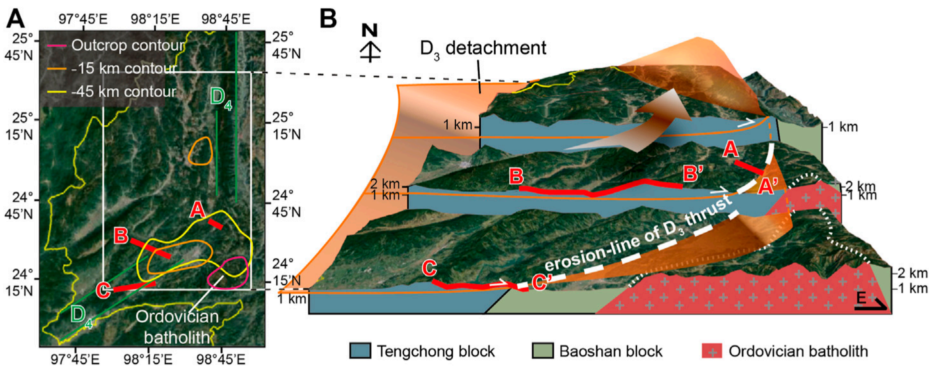

FIGURE 10
Satellite image and 3D-block topography diagram showing major structures and geological units around the Gaoligong orocline. **(A)** Satellite image shows the location of the high-resistivity Ordovician basement (Ye et al., 2020). The red line marks the surface exposure of the Ordovician basement, the orange line marks the boundary at a depth of 15 km, and the yellow line marks the boundary at a depth of 45 km. The green line marks the strike of D_4 shear belts. **(B)** 3D-block diagram showing the curvature of the Gaoligong orocline produced by intersecting the topography surface to the shoveled shape thrust shear plane against the Ordovician batholith.

the Gaoligong orogeny to the regional tectonic evolution, we consider that the formation of the Gaoligong orocline occurred during 40 Ma–28 Ma during a D_3 deformation event.

4.2 Structural geometry influenced by the Ordovician basement

The Tengchong block was accreted to the Baoshan block before the late Cretaceous (Xu et al., 2012; Gardiner et al., 2018). After suturing, these two micro-blocks should have similar structural characteristics as they were under the same tectonic settings: 1) Neo-Tethyan subduction and 2) the India–Eurasia continent–continent collision. However, according to our reconstruction results, the D_3 fold-thrust-belt only developed in the Tengchong block and not in the Baoshan block, suggesting a considerable difference between these two blocks or the presence of some structural barrier to prevent strain from propagating. The Baoshan block is covered by Paleozoic and Mesozoic strata (Akciz et al., 2008) with sporadic intrusion and has a crustal thickness of 30 km–35 km (Zhang and Gao, 2019). On the other hand, the Tengchong block has a relatively thick crust (35 km–40 km) and was repeatedly intruded during 78 Ma–40 Ma (Figure 9; Xu et al., 2008; Xu et al., 2012; Ma et al., 2014; Chen et al., 2015; Xie et al., 2016; Zhang et al., 2017; Zhang and Gao, 2019). The magnetotelluric analysis shows a high-resistivity zone extending through the entire crust beneath the Ordovician basement (Figures 2B and Figure 10; Ye et al., 2020). The collocation of the Tengchong block–Ordovician basement–Baoshan block is similar to the Songpan–Ganzi–Longmenshan–Sichuan basin (Zhao et al., 2012; Wang et al., 2014). Zhao et al. (2012) revealed that the rigid high-resistivity lithosphere blocks the east-directed mid-crustal level flow beneath Longmenshan. Although the tectonic scales of the two localities are different, the concept that an ancient structure, the Proto-Tethys-related Ordovician basement, can stop the strain of D_3 from working on the Baoshan block is consistent between them.

The location of the high-resistivity regions of the Ordovician basement at a depth of 20 km is shown in Figure 10A. The convex shape of the Gaoligong orocline is clear (Ye et al., 2020), but extends beneath the Tengchong block at a depth of middle-to-lower crust (the depth of 15 km and 45 km contours of Figure 10A; Ye et al., 2020). It appears that the Ordovician basement provided a rigid ramp as a footwall for oblique thrusting and resulted in heterogeneous deformation of D_3 in the middle crust (e.g., sample 14CG12; Figure 10B). The Ordovician basement also affected all younger deformation events of the Tengchong block, such as blocking the extension of the N-S-trending GLSZ (red line of Figure 10A) and NE-SW trending D_4 shear zone (green line of Figure 10A). As a response to the accumulated stress (Zhao et al., 2012; Ye et al., 2020), the post-orogeny collapse (D_5) was accompanied by erosion and the development from the south of the Gaoligong mountain to the north after 15 Ma (G. Wang et al., 2006a).

4.3 The formation mechanism of the Gaoligong orocline

The typical formation mechanisms of oroclines can be subdivided into non-rotational (primary) and rotational oroclines (secondary; Figure 1A). According to our reconstruction, no secondary deformation event altered the geometry of the Gaoligong orocline. Thus, we can say that the Gaoligong orocline is more likely to fall within the category of non-rotational (primary) oroclines. The primary orocline is mostly restricted to thin-skinned thrust belts that reflect the plate boundary's original curvature, resulting in one stage of foliation development (e.g., Marshak, 1988; 2005; Weil and Sussman, 2004; Johnston et al., 2013). Based on the lithology distribution, the Gaoligong orocline also marks the boundary between the Tengchong and Baoshan blocks, making it a suitable block setting for developing a non-rotational orocline. In such a case, radial fan foliations that strike parallel to the trend of the orocline should be expected for the syn-orocline-forming event, which would be S/C and S_3 for the Gaoligong orocline. From our field measurements, only NW-SE-striking foliations but not NE-SW-striking foliations are found for the D_3 event. Mechanism 2 is very similar to our reconstructed style, but the indenter, which is the Ordovician basement of the Baoshan block, is situated on the site opposite to the orocline. The wrong geographic position of the indenter and lack of orocline parallel striking foliations argue against the possibility of a primary orocline for the forming mechanism of the Gaoligong orocline. Therefore, we conclude that the Gaoligong orocline is an "atypical" orocline and that the curved geometry along the Tengchong block boundary is a visual effect due to the intersection of the shovel-like thrust belt to the topographically relieved surface.

5 Conclusion

Based on our structural reconstruction, five deformation events were reconstructed for the southern section of the Gaoligong orocline. By correlating the structural evolution between the northern and southern sections, we conclude that the Gaoligong orocline underwent the same deformation event since D_3. All D_4 and D_5 structures show orocline parallel foliation, indicating that they had reused the orocline geometry during deformation. Therefore, the D_4 and D_5 events occurred after the formation of the orocline, leaving D_3 as the most probable candidate for orocline formation during the India–Asia hard collision (40–28 Ma). Since D_4 and D_5 do not show progressive deformation to further develop the curvature of the orocline, we can reject the Gaoligong orocline formed by rotational oroclinal development. Although the thrust belt of D_3 is the major forming mechanism of the Gaoligong orocline, the Ordovician basement behaved as an "indenter" that controlled the geometry of this thrust front. In addition, the radial fan pattern that follows the orocline of the S_3 foliations cannot be observed. Furthermore, according to the primary orocline model, the "indenter" should be situated to the west of the concave orocline, but the Ordovician basement between the Tengchong and Baoshan blocks is situated to the east of the orocline, leading us to reject the hypothesis that the Gaoligong orocline was formed by non-rotational oroclinal development. The geometry of the Gaoligong orocline does not reflect a "bended orogeny," but a visual effect of topography relief over a shovel-like thrusting plane; thus, it is an "atypical" orocline.

Data availability statement

The original contributions presented in the study are included in the article/Supplementary Material; further inquiries can be directed to the corresponding author.

Author contributions

All authors, Y-PC, M-WY, and T-YL, conducted the field study and sample collection of this manuscript together. Y-PC was responsible for sample analysis, structural reconstruction, and manuscript writing. M-WY and T-YL were responsible for data discussion and manuscript editing and revision.

Funding

This study was financially supported by the National Science Council, Taiwan, ROC, under grant numbers National Science Council 102–2116 M003 and NSC 99–2116 M003.

Acknowledgments

We thank Y.Z. Xu and Y.L. Lin for their help in the field. We thank Greg Shellnutt for the final English proofreading.

Conflict of interest

The authors declare that the research was conducted in the absence of any commercial or financial relationships that could be construed as a potential conflict of interest.

Publisher's note

Supplementary material

The Supplementary Material for this article can be found online at: https://www.frontiersin.org/articles/10.3389/feart.2023.1075043/full#supplementary-material

References

Aitken, J. D., and Long, D. G. F. (1978). Mackenzie tectonic arc-Reflection of early basin configuration? *Geology* 6 (10), 626–629. doi:10.1130/0091-7613(1978)6<626:MTAOEB>2.0.CO;2

Akciz, S., Burchfiel, B. C., Crowley, J. L., Jiyun, Y., and Liangzhong, C. (2008). Geometry, kinematics, and regional significance of the chong Shan shear zone, eastern himalayan syntaxis, yunnan, China. *Geosphere* 4, 292–314. doi:10.1130/GES00111.1

Bajolet, F., Replumaz, A., and Lainé, R. (2013). Orocline and syntaxes formation during subduction and collision. *Tectonics* 32 (5), 1529–1546. doi:10.1002/tect.20087

Barrow, G. (1893). On an intrusion of muscovite-biotite gneiss in the south-eastern highlands of scotland, and its accompanying metamorphism. *Quart. J. Geol. Soc. Lond.* 49 (1-4), 330–358. doi:10.1144/GSL.JGS.1893.049.01-04.52

Bendick, R., and Bilham, R. (2001). How perfect is the Himalayan arc? *Geology* 29 (9), 791–794. doi:10.1130/0091-7613(2001)029<0791:HPITHA>2.0.CO;2

Bersan, S. M., Danderfer, A., Lagoeiro, L., and Costa, A. F. O. (2017). The kinematic evolution of the serra central salient, eastern Brazil: A neoproterozoic progressive arc in northern espinhaço fold-thrust belt. *J. South Am. Earth Sci.* 80, 131–148. doi:10.1016/j.jsames.2017.09.013

BGMRYP (1983). *Geological map of yunnan, scale 1:1,000,000 scale*. Kunming: Bureau of Geology and Mineral Resources of Yunnan Province.

Burchfiel, B. C. (2004). 2003 presidential address: New technology; new geological challenges. *GSA Today* 14, 4–10. doi:10.1130/1052-5173(2004)014<4:panngc>2.0.co;2

Capitanio, F. A., Faccenna, C., Zlotnik, S., and Stegman, D. R. (2011). Subduction dynamics and the origin of Andean orogeny and the Bolivian orocline. *Nature* 480, 83–86. doi:10.1038/nature10596

Carey, S. W. (1955). The orocline concept in geotectonics-Part I. *Pap. Proc. - R. Soc. tasman.* 89, 255–288.

Cawood, P. A. (2022). Untangling the history of oroclines and mountain belts. *Natl. Sci. Rev.* 9 (5), nwab211. doi:10.1093/nsr/nwab211

Chen, X. C., Hu, R. Z., Bi, X. W., Zhong, H., Lan, J. B., Zhao, C. H., et al. (2015). Petrogenesis of metaluminous A-type granitoids in the Tengchong–Lianghe tin belt of southwestern China: Evidences from zircon U–Pb ages and Hf–O isotopes, and whole-rock Sr–Nd isotopes. *Lithos* 212-215, 93–110. doi:10.1016/j.lithos.2014.11.010

Chiu, Y. P., Yeh, M. W., Wu, K. H., Lee, T. Y., Lo, C. H., Chung, S. L., et al. (2018). Transition from extrusion to flow tectonism around the Eastern Himalaya syntaxis. *Geol. Soc. Am. Bull.* 130 (9-10), 1675–1696. doi:10.1130/B31811.1

Chung, S. L., Chu, M. F., Zhang, Y. Q., Xie, Y. W., Lo, C. H., Lee, T. Y., et al. (2005). Tibetan tectonic evolution inferred from spatial and temporal variations in post-collisional magmatism. *Earth. Sci. Rev.* 68, 173–196. doi:10.1016/j.earscirev.2004.05.001

Clark, M. K., and Royden, L. H. (2000). Topographic ooze: Building the eastern margin of Tibet by lower crustal flow. *Geology* 28 (8), 703–706. doi:10.1130/0091-7613(2000)028<0703:tobtem>2.3.co;2

Dan, W., Murphy, J. B., Tang, G. J., Zhang, X. Z., White, W. M., and Wang, Q. (2022). Cambrian–Ordovician magmatic flare-up in NE Gondwana: A silicic large igneous province? *GSA Bull.* doi:10.1130/B36331.1

Eroğlu, S., Siebel, W., Danišík, M., Pfänder, J. A., and Chen, F. K. (2013). Multi-system geochronological and isotopic constraints on age and evolution of the Gaoligongshan metamorphic belt and shear zone system in Western Yunnan, China. *J. Asian Earth Sci.* 73, 218–239. doi:10.1016/j.jseaes.2013.03.031

Fergusson, C. L. (2019). Subduction accretion and orocline development in modern and ancient settings: Implications of Japanese examples for development of the New England Orogen of eastern Australia. *J. Geodyn.* 129, 117–130. doi:10.1016/j.jog.2017.11.008

Gardiner, N. J., Searle, M. P., Morley, C. K., Robb, L. J., Whitehouse, M. J., Roberts, N. M. W., et al. (2018). The crustal architecture of Myanmar imaged through zircon U-Pb, Lu-Hf and O isotopes: Tectonic and metallogenic implications. *Gondwana Res.* 62, 27–60. doi:10.1016/j.gr.2018.02.008

Gutiérrez-Alonso, G., Fernández-Suárez, J., and Weil, A. B. (2004). "Orocline triggered lithospheric delamination," in *Orogenic curvature: Integrating paleomagnetic and structural analyses*. Editors A. J. Sussman and A. B. Weil (Colorado: Geological Society of America), 121–131. doi:10.1130/0-8137-2383-3(2004)383[121:OTLD]2.0.CO;2

Gutierrez-Alonso, G., Johnston, S., Weil, A., Pastor-Galán, D., and Fernández-Suárez, J. (2012). Buckling an orogen: The cantabrian orocline. *GSA Today* 22, 4–9. doi:10.1130/GSATG141A.1

Harrison, T. M., Duncan, I., and McDougall, I. (1985). Diffusion of ^{40}Ar in biotite: Temperature, pressure and compositional effects. *Geochim. Cosmochim. Acta* 49 (11), 2461–2468. doi:10.1016/0016-7037(85)90246-7

Harrison, T. M., and McDougall, I. (1982). The thermal significance of potassium feldspar K-Ar ages inferred from age spectrum results. *Geochim. Cosmochim. Ac.* 46 (10), 1811–1820. doi:10.1016/0016-7037(82)90120-X

He, X., Zhou, R., Tan, S., Liu, Z., Wang, G., Jiang, Z., et al. (2021). Late Cretaceous–Eocene magmatism induced by slab rollback and breakoff in the Tengchong terrane, SW China. *Int. Geol. Rev.* 63 (3), 294–316. doi:10.1080/00206814.2019.1709567

Hwang, B. H., Son, M., Kim, J. S., Yang, K., and Kim, J. S. (2012). Cenozoic wrench tectonics and oroclinal bending in SE Korea. *Int. Geol. Rev.* 54 (6), 642–653. doi:10.1080/00206814.2011.562389

Johnston, S. T., Weil, A. B., and Gutiérrez-Alonso, G. (2013). Oroclines: Thick and thin. *Geol. Soc. Am. Bull.* 125, 643–663. doi:10.1130/B30765.1

Klootwijk, C. T., Conaghan, P. J., and McA Powell, C. (1985). The himalayan arc: Large-scale continental subduction, oroclinal bending and back-arc spreading. *Earth Planet. Sci. Lett.* 75 (2), 167–183. doi:10.1016/0012-821X(85)90099-8

Lawrence, R. D., Yeats, R. S., Khan, S. H., Subhani, A. M., and Bonelli, D. (1981). Crystalline rocks of the Spinatizha area, Pakistan. *J. Struct. Geol.* 3 (4), 449–457. doi:10.1016/0191-8141(81)90044-4

Li, G. J., Wang, Q. F., Huang, Y. H., Gao, L., and Yu, L. (2016). Petrogenesis of middle Ordovician peraluminous granites in the Baoshan block: Implications for the early Paleozoic tectonic evolution along East Gondwana. *Lithos* 245, 76–92. doi:10.1016/j.lithos.2015.10.012

Liu, G., Sun, Z., Zi, J., Santosh, M., Zhao, T., Feng, Q., et al. (2021). Proto-Tethys ophiolitic mélange in SW Yunnan: Constraints from zircon U-Pb geochronology and geochemistry. *Geosci. Front.* 12 (5), 101200. doi:10.1016/j.gsf.2021.101200

Liu, S., Hu, R. Z., Gao, S., Feng, C. X., Huang, Z., Lai, S., et al. (2009). U–Pb zircon, geochemical and Sr–Nd–Hf isotopic constraints on the age and origin of early palaeozoic I-type granite from the tengchong–baoshan block, western yunnan province, SW China. *J. Asian Earth Sci.* 36 (2), 168–182. doi:10.1016/j.jseaes.2009.05.004

Ma, L., Wang, Y., Fan, W., Geng, H., Cai, Y., Zhong, H., et al. (2014). Petrogenesis of the early Eocene I-type granites in west Yingjiang (SW Yunnan) and its implication for the eastern extension of the Gangdese batholiths. *Gondwana Res.* 25, 401–419. doi:10.1016/j.gr.2013.04.010

Macedo, J., and Marshak, S. (1999). Controls on the geometry of fold-thrust belt salients. *GSA Bull.* 111 (12), 1808–1822. doi:10.1130/0016-7606(1999)111<1808:COTGOF>2.3.CO;2

Marshak, S. (1988). Kinematics of orocline and arc formation in thin-skinned orogens. *Tectonics* 7 (1), 73–86. doi:10.1029/TC007i001p00073

Marshak, S. (2005). Salients, recesses, arcs, oroclines, and syntaxes - a review of ideas concerning the formation of map-view curves in fold-thrust belts. *AAPG Mem.* 82, 131–156. doi:10.1306/M82813C9

Martínez Catalán, J. R. (2011). Are the oroclines of the Variscan belt related to late Variscan strike-slip tectonics? *Terra nova.* 23, 241–247. doi:10.1111/j.1365-3121.2011.01005.x

Martínez Catalán, J. R. (2012). The Central Iberian arc, an orocline centered in the Iberian Massif and some implications for the Variscan belt. *Int. J. Earth Sci.* 101 (5), 1299–1314. doi:10.1007/s00531-011-0715-6

Metcalfe, I. (2013). Gondwana dispersion and Asian accretion: Tectonic and palaeogeographic evolution of eastern Tethys. *J. Asian Earth Sci.* 66 (0), 1–33. doi:10.1016/j.jseaes.2012.12.020

Metcalfe, I. (1996). Gondwanaland dispersion, Asian accretion and evolution of eastern Tethys. *Aust. J. Earth Sci.* 43 (6), 605–623. doi:10.1080/08120099608728282

Mitchell, A. H. G. (1993). Cretaceous–Cenozoic tectonic events in the Western Myanmar (Burma)–Assam region. *J. Geol. Soc. Lond.* 150 (6), 1089–1102. doi:10.1144/gsjgs.150.6.1089

Mitchell, A. H. G., Hlaing, T., and Oo, T. (2008). "Possible jurassic collision within the Shan-Thai block in central Myanmar: Continuation of the shengza suture in tibet?" in *International conference on tectonics of northwestern Indochina abstract volum*. Editors S. Chantraprasert, O. Limtrakun, and Compilers (Chiang Mai, Thailand), 23–24.

Morley, C. K., and Arboit, F. (2019). Dating the onset of motion on the Sagaing fault: Evidence from detrital zircon and titanite U-Pb geochronology from the North Minwun Basin, Myanmar. *Geology* 47 (6), 581–585. doi:10.1130/G46321.1

Muñoz, J. A., Beamud, E., Fernández, O., Arbués, P., Dinarès-Turell, J., and Poblet, J. (2013). The Ainsa Fold and thrust oblique zone of the central Pyrenees: Kinematics of a curved contractional system from paleomagnetic and structural data. *Tectonics* 32 (5), 1142–1175. doi:10.1002/tect.20070

Owona, S., Ondoa, J. M., and Ekodeck, G. E. (2013). Evidence of quartz, feldspar and amphibole crystal plastic deformations in the paleoproterozoic nyong complex shear zones under amphibolite to granulite conditions (west central african fold belt, SW Cameroon). *J. Geol. Geogr.* 5 (3), 186–201. doi:10.5539/jgg.v5n3p186

Passchier, C. W., and Trouw, R. A. J. (1996). *Microtectonics.* Berlin: Springer-Verlag, 289.

Patiño Douce, A. E., Humphreys, E. D., and Johnston, A. D. (1990). Anatexis and metamorphism in tectonically thickened continental crust exemplified by the Sevier hinterland, Western North America. *Earth Planet. Sci. Lett.* 97, 290–315. doi:10.1016/0012-821x(90)90048-3

Qi, X., Wei, C., Zhang, C., Zhang, S., Hu, Z., and Ji, F. (2019). Southward extension of the bangonghu–nujiang suture: Evidence from early cretaceous intermediate and felsic magmatism in the Gaoligong orogen, China. *J. Asian Earth Sci.* 175, 1–25. doi:10.1016/j.jseaes.2018.09.007

Royden, L. H., Burchfiel, B. C., King, R. W., Wang, E., Chen, Z., Shen, F., et al. (1997). Surface deformation and lower crustal flow in eastern Tibet. *Science* 276, 788–790. doi:10.1126/science.276.5313.788

Sacchi, R., and Cadoppi, P. (1988). Oroclines and pseudo-oroclines. *Tectonophysics* 146 (1), 47–58. doi:10.1016/0040-1951(88)90080-7

Searle, M. P., Noble, S. R., Cottle, J. M., Waters, D. J., Mitchell, A. H. G., Hlaing, T., et al. (2007). Tectonic evolution of the Mogok metamorphic belt, Burma (Myanmar) constrained by U-Th-Pb dating of metamorphic and magmatic rocks. *Tectonics* 26 (3), TC3014. doi:10.1029/2006TC002083

Shi, M. F., Lin, F. C., Li, Z., Ling, X. M., and Shi, H. Z. (2011). Stratigraphic zoning and tectonic events in Indochina and adjacent areas of southwest China. *Geol. China* 38 (5), 1244–1256.

Sone, M., and Metcalfe, I. (2008). Parallel tethyan sutures in mainland southeast asia: New insights for palaeo-tethys closure and implications for the indosinian orogeny. *CR Geosci.* 340 (2–3), 166–179. doi:10.1016/j.crte.2007.09.008

Song, S. G., Niu, Y. L., Wei, C. J., Ji, J. Q., and Su, L. (2010). Metamorphism, anatexis, zircon ages and tectonic evolution of the Gongshan block in the northern Indochina continent- an eastern extension of the Lhasa Block. *Lithos* 120, 327–346. doi:10.1016/j.lithos.2010.08.021

Sun, Z., Dong, G., Santosh, M., Mo, X., Dong, P., Wang, W., et al. (2020). A Late Cretaceous felsic magmatic suite from the Tengchong Block, Western Yunnan: Integrated geochemical and isotopic investigation and implications for Sn mineralization. *Geol. Mag.* 157 (8), 1316–1332. doi:10.1017/S0016756819001493

Wang, G., Wan, J., and Wang, E. (2006a). Extensional collapse of the southern part of the Gaoligong range in the western yunnan, China and its tectonic origin. *Acta Geol. Sin.* 80 (9), 1262–1273. doi:10.3321/j.issn:0001-5717.2006.09.004

Wang, X., Zhang, G., Fang, H., Luo, W., Zhang, W., Zhong, Q., et al. (2014). Crust and upper mantle resistivity structure at middle section of Longmenshan, eastern Tibetan plateau. *Tectonophysics* 619-620, 143–148. doi:10.1016/j.tecto.2013.09.011

Wang, Y. J., Fan, W. M., Zhang, Y. H., Peng, T. P., Chen, X. Y., and Xu, Y. G. (2006b). Kinematics and ^{40}Ar/^{39}Ar geochronology of the Gaoligong and Chongshan shear systems, Western Yunnan, China: Implications for early Oligocene tectonic extrusion of SE Asia. *Tectonophysics* 418, 235–254. doi:10.1016/j.tecto.2006.02.005

Wang, Y., Xing, X., Cawood, P. A., Lai, S., Xia, X., Fan, W., et al. (2013). Petrogenesis of early Paleozoic peraluminous granite in the Sibumasu Block of SW Yunnan and diachronous accretionary orogenesis along the northern margin of Gondwana. *Lithos* 182-183, 67–85. doi:10.1016/j.lithos.2013.09.010

Weil, A. B., Van der Voo, R., and Van der Pluijm, B. A. (2001). Oroclinal bending and evidence against the Pangea megashear: The Cantabria-Asturias arc (northern Spain). *Geology* 29 (11), 991–994. doi:10.1130/0091-7613(2001)029<0991:OBAEAT>2.0.CO;2

Weil, A., and Sussman, A. (2004). Classifying curved orogens based on timing relationships between structural development and vertical-axis rotations. *Spec. Pap. Geol. Soc. Am.* 383, 1–17. doi:10.1130/0-8137-2383-3(2004)383[1:CCOBOT]2.0.CO;2

Wopfner, H. (1996). Gondwana origin of the baoshan and Tengchong terranes of West Yunnan. *Geol. Soc. Spec. Publ.* 106 (1), 539–547. doi:10.1144/gsl.sp.1996.106.01.34

Xie, J. C., Zhu, D. C., Dong, G., Zhao, Z., Wang, Q., and Mo, X. (2016). Linking the Tengchong terrane in SW yunnan with the lhasa terrane in southern tibet through magmatic correlation. *Gondwana Res.* 39, 217–229. doi:10.1016/j.gr.2016.02.007

Xu, Y. G., Lan, J. B., Yang, Q. J., Huang, X. L., and Qiu, H. N. (2008). Eocene break-off of the Neo-Tethyan slab as inferred from intraplate-type mafic dykes in the Gaoligong orogenic belt, eastern Tibet. *Chem. Geol.* 255 (3–4), 439–453. doi:10.1016/j.chemgeo.2008.07.016

Xu, Y. G., Yang, Q. J., Lan, J. B., Luo, Z. Y., Huang, X. L., Shi, Y. R., et al. (2012). Temporal–spatial distribution and tectonic implications of the batholiths in the Gaoligong–Tengliang–Yingjiang area, Western Yunnan: Constraints from zircon U–Pb ages and Hf isotopes. *J. Asian Earth Sci.* 53, 151–175. doi:10.1016/j.jseaes.2011.06.018

Xu, Z., Wang, Q., Cai, Z., Dong, H., Li, H., Chen, X., et al. (2015). Kinematics of the Tengchong Terrane in SE Tibet from the late Eocene to early Miocene: Insights from coeval mid-crustal detachments and strike-slip shear zones. *Tectonophysics* 665, 127–148. doi:10.1016/j.tecto.2015.09.033

Yamaoka, K., Fukao, Y., and Kumazawa, M. (1986). Spherical shell tectonics: Effects of sphericity and inextensibility on the geometry of the descending lithosphere. *Rev. Geophys.* 24 (1), 27–53. doi:10.1029/RG024i001p00027

Ye, T., Chen, X., Huang, Q., Zhao, L., Zhang, Y., and Uyeshima, M. (2020). Bifurcated crustal channel flow and seismogenic structures of intraplate earthquakes in western yunnan, China as revealed by three-dimensional magnetotelluric imaging. *J. Geophys. Res. Solid Earth* 125 (9), e2019JB018991. doi:10.1029/2019JB018991

Yeh, M. W., and Bell, T. H. (2004). Significance of dextral reactivation of an E-W transfer fault in the formation of the Pennsylvania orocline, central Appalachians. *Tectonics* 23 (5), TC5009. doi:10.1029/2003TC001593

Zhang, B., Chai, Z., Yin, C. Y., Huang, W. T., Wang, Y., Zhang, J. J., et al. (2017). Intra-continental transpression and gneiss doming in an obliquely convergent regime in SE Asia. *J. Struct. Geol.* 97, 48–70. doi:10.1016/j.jsg.2017.02.010

Zhang, Z., and Gao, Y. (2019). Crustal thicknesses and Poisson's ratios beneath the chuxiong-simao basin in the southeast margin of the Tibetan plateau. *Earth Planet. Sci. Lett.* 3, 69–84. doi:10.26464/epp2019008

Zhao, G., Unsworth, M. J., Zhan, Y., Wang, L., Chen, X., Jones, A. G., et al. (2012). Crustal structure and rheology of the Longmenshan and Wenchuan Mw 7.9 earthquake epicentral area from magnetotelluric data. *Geology* 40 (12), 1139–1142. doi:10.1130/G33703.1

Zhao, S. W., Lai, S. C., Gao, L., Qin, J. F., and Zhu, R. Z. (2017). Evolution of the proto-tethys in the baoshan block along the east Gondwana margin: Constraints from early palaeozoic magmatism. *Int. Geol. Rev.* 59, 1–15. doi:10.1080/00206814.2016.1198994

Zhao, S. W., Lai, S. C., Qin, J. F., and Zhu, R. Z. (2014). Zircon U-Pb ages, geochemistry, and Sr-Nd-Pb-Hf isotopic compositions of the pinghe pluton, southwest China: Implications for the evolution of the early palaeozoic proto-tethys in southeast asia. *Int. Geol. Rev.* 56 (7), 885–904. doi:10.1080/00206814.2014.905998